

## Supplementary Materials for

### Nanoscale Lamb wave–driven motors in nonliquid environments

Jinsheng Lu, Qiang Li, Cheng-Wei Qiu, Yu Hong, Pintu Ghosh, Min Qiu\*

\*Corresponding author. Email: [minqiu@zju.edu.cn](mailto:minqiu@zju.edu.cn), [qiu\\_lab@westlake.edu.cn](mailto:qiu_lab@westlake.edu.cn)

Published 8 March 2019, *Sci. Adv.* **5**, eaau8271 (2019)

DOI: 10.1126/sciadv.aau8271

#### The PDF file includes:

Section S1. Measurements of the adhesion force between gold plates and microfibers  
Section S2. Extraction of the angle between gold plates and microfibers  
Section S3. Ruling out the optical force and the photophoretic force as driving forces  
Section S4. A theoretical model of locomotion resolution  
Section S5. Numerical simulations of the Lamb wave in an asymmetrically configured plate  
Fig. S1. Experimental procedures.  
Fig. S2. Experimental configuration of the locomotor system in vacuum.  
Fig. S3. Numerical calculation of plasmonic heating in the gold plate.  
Fig. S4. Measurements of the adhesion force between gold plates and microfibers.  
Fig. S5. Calculations of the angle between the gold plate and the microfiber using the projection method.  
Fig. S6. Rotation of the locomotor actuated by light pulses with different repetition rates.  
Fig. S7. Experimental system of a micromirror for optical sweeping.  
Fig. S8. Numerical results of the Lamb wave generated in a gold plate.  
Fig. S9. Wave motion patterns for the right-shifted and left-shifted asymmetric configurations.  
Fig. S10. Lamb wave propagating in a larger gold plate.  
Legends for movies S1 to S10  
References (32–41)

#### Other Supplementary Material for this manuscript includes the following:

(available at [advances.sciencemag.org/cgi/content/full/5/3/eaau8271/DC1](https://advances.sciencemag.org/cgi/content/full/5/3/eaau8271/DC1))

Movie S1 (.mp4 format). A motor that is driven by a pulsed supercontinuum light with different repetition rates in air (sample A).  
Movie S2 (.mp4 format). A motor that is driven by a pulsed supercontinuum light in vacuum.  
Movie S3 (.mp4 format). A pulsed light–actuated stepping motor.

Movie S4 (.mp4 format). A lower power of the light pulse and a smaller rotation step for the locomotor.

Movie S5 (.mp4 format). A motor that is driven by a 1064-nm pulsed light in air.

Movie S6 (.mp4 format). A motor that is driven by a pulsed supercontinuum light with different repetition rates in air (sample B).

Movie S7 (.mp4 format). Deforming the microfiber to measure the adhesion force.

Movie S8 (.mp4 format). An animation to illustrate the rotary locomotion of the motor.

Movie S9 (.mp4 format). A light-actuated rotary micromirror.

Movie S10 (.mp4 format). Rotation direction of the motor controlled by different asymmetric configurations.

## **Section S1. Measurements of the adhesion force between gold plates and microfibers**

From the experiment results, the adhesion force between gold plates and microfibers has two characteristics: (i) It is a dry adhesion which behaves far stronger in air compared with that in liquid environments. Our experiments show that the gold plate no longer adheres to the microfiber in liquid environments. (ii) It is non-directional (i.e. the adhesion force prevents the plate from leaving the microfiber surface in any direction). For example, in the radial direction (i.e. perpendicular to the contact surface), the adhesion force works as an attractive centripetal force to keep the gold plate in contact with the microfiber tightly. In the azimuthal direction (parallel to the contact surface), the adhesion force acts as a friction force to prevent the gold plate from sliding on the surface of the microfiber. According to these two characteristics, this adhesion force can be contributed to the well-known van der Waals force.

In order to measure this adhesion force, we use a tapered fiber probe to touch the gold plate which is placed on the microfiber (movie S7, fig. S4C). The gold plate is also stuck to the probe due to the adhesion. When the probe (attached with the gold plate) is moved slowly to the left, the gold plate also moves to the left with the probe. The adhesion force (between the gold plate and the microfiber) in the azimuthal direction, which acts as friction force, pulls the microfiber and causes the microfiber to bend. The probe moves slowly. Therefore it can be considered as a force-balanced model. The plate gets detached from the microfiber when the force applied on the plate by the microfiber due to bending is greater than this friction force (fig. S4D). After that, the microfiber restores back to its initial position (fig. S4E). The adhesion force in the azimuthal direction (i.e. the friction force) is equal to the maximum bending force of the microfiber (fig. S4F), which can be calculated from the elastic deformation model of the microfiber (fig. S4G) (Note that the tension of the microfiber in this model is not considered. If the tension of the microfiber is taken into consideration, the estimated force will be larger). Since the displacement

$\Delta x$  is far smaller than the length of the microfiber  $L$ , the elastic force ( $F$ ) and the pulling force ( $F_x$ ) can be calculated by using the following formula (32)

$$F_x = 2F \cdot \cos(\theta) = 2 \frac{E \cdot S}{L/2} \left( \Delta x - \frac{L}{2} \frac{\Delta x}{\sqrt{\Delta x^2 + L^2/4}} \right) \quad (1)$$

The displacement  $\Delta x$  measured in the experiment is 10  $\mu\text{m}$ . The length  $L$  and the effective diameter  $d$  of the microfiber used in the experiment are 14 mm and 36  $\mu\text{m}$ , respectively (fig. S4, A and B). Young's modulus  $Y$  of silica is 73.1 GPa. The calculated pulling force  $F_x$  is 6.9  $\mu\text{N}$  for the maximum displacement. Thus the azimuthal adhesion force between the gold plate and the microfiber is estimated to be 6.9  $\mu\text{N}$ , while the gravitational force of the gold plate (side length 11  $\mu\text{m}$ , thickness 30 nm, and density 19.3  $\text{g/cm}^3$ ) is only 1.8 pN ( $G = \rho V g = 1.8 \times 10^{-12} \text{ N}$ ).

According to the non-directional characteristic of this adhesion force, adhesion force in the radial direction should also be in the range of  $\mu\text{N}$ .

We also use the formula of van der Waals force to estimate this adhesion force theoretically. The van der Waals force is a short range force, the origin of which comes from instantaneous dipole due to the fluctuation of the electron cloud. The van der Waals force for the cylinder-planar surface can be estimated as (33)

$$F = \frac{A \cdot L \cdot d^{1/2}}{16 z_0^{5/2}} \quad (2)$$

where  $A$  is the Hamaker constant;  $d$  is the diameter of the cylinder;  $z_0$  is the separation distance between the cylinder and the planar surface;  $L$  is the length of the cylinder contacted with the planar surface. Hamaker constant for gold and silica in vacuum are  $40 \times 10^{-20} \text{ J}$  and  $6.5 \times 10^{-20} \text{ J}$ , respectively. In case of two different materials contacted with each other, the Hamaker constant  $A$

is calculated as  $2 \cdot (A_{gold} \cdot A_{silica}) / (A_{gold} + A_{silica}) = 11.2 \times 10^{-20}$  J. Diameter of the microfiber which is in contact with the gold plate is 2  $\mu\text{m}$ . Contact length is about 15  $\mu\text{m}$ . The van der Waals force comes out to be 4.7  $\mu\text{N}$  for a separation distance of 1 nm, which is roughly consistent with the measured result of 6.9  $\mu\text{N}$ .

## Section S2. Extraction of the angle between gold plates and microfibers

All the experiment videos are recorded from the top view as shown in fig. S5A. During rotation of the gold plate, the area of the gold plate shown in the videos changes periodically over time. The angle between the gold plate and microfiber can be calculated from the area of the gold plate (fig. S5B). We use image processing methods to extract the outline of the gold plate in every frame of the experiment videos and calculate the area  $A$  ( $A'$ ) of the gold plate. For convenient, the size of the gold plate is presented with pixel length and the unit of area of the gold plate is *square of pixel* ( $\text{pixel}^2$ ). The angle is then calculated as  $\theta = a \cos(\sqrt{A' / A})$  and the effective width of the gold plate is obtained as  $W_{eff} = \sqrt{A} \cos(\theta)$ .

## Section S3. Ruling out the optical force and the photophoretic force as driving forces

In our experiments, continuous wave (CW) lasers with wavelength 532 nm, 980 nm, and 1,064 nm are also tried, but the rotation of the gold plate does not happen. In contrast, a pulsed laser with a single wavelength (e.g., 1064 nm) or broadband wavelength (e.g., supercontinuum light) can drive the gold plate to rotate. For the mechanism of this light-induced rotation, the optical force and the photophoretic force, which are the two most basic light-induced forces, should be taken into consideration firstly. In our previous work (18), it is shown that the photophoretic force synergized with the optical force can pull and push a gold plate on a tapered fiber. However, these two forces can be ruled out as driving forces for the rotation in our present experiments.

First, the photophoretic force arises as a result of the surrounding gas molecules interacting with objects that have a nonzero temperature gradient. The gas molecules bounce at the hot side of objects with greater velocity compared with that at the cold side. It generates a net force to objects (34). The photophoretic force is proportional to gas pressure (35). In our experiments, light-induced rotation can also happen in the vacuum (SEM chamber), where the gas pressure is about 9 orders of magnitude lower than that in the air environment. In light of this, the photophoretic force can be neglected in the vacuum. Thus the photophoretic force is expected not to be the main reason for this light-induced rotation. Although the photophoretic effect is not the main cause of the rotation, it is expected that it would play a role in some cases. When the laser power is too high (i.e. higher repetition rate or higher pulse energy), the photophoretic force would become obvious. In one experiment, the gold plate bounces off the microfiber when the maximum average power of the laser (20 mW) is used. It is expected to be due to the photophoretic force in the direction perpendicular to the long axis of the microfiber. This force can cause the gold plate to jump off the microfiber. When the experiment is conducted in the vacuum and the laser power is too high, the gold plate does not jump off the microfiber. It melts on the microfiber. Note that another main observed difference between experiments in the air and in the vacuum is that the heat in the vacuum is more easily accumulated to raise the temperature of the gold plate high if the experiment runs for a long time, causing the damage of the gold plate. The plasmonic heating will prevent the rotation of the motor from reaching a high speed. Besides, the influence of air viscous drag is not obvious in our experiments at present due to the small rotation speed of the motor (the highest rotation speed of the gold plate currently achieved is  $\sim 130$  rpm). It is expected that the influence of the air would become obvious when a pulsed laser with higher repetition rate is used and the motor reaches a high rotation speed.

Second, the optical force is a direct photon-matter interaction force which does not need surrounding (air) molecules. Therefore it cannot be neglected even in vacuum. However, one can

rule out the optical force for causing the rotation with the following reasons. (i) If the optical force is the driving force, the rotation should also happen for a CW laser with high enough power comparable to the pulsed laser power. However, our experiments show that the rotation phenomenon does not happen when a CW laser is used even though the laser power is high enough to melt the plate. (ii) Experiment results show that the rotation direction of the gold plate does not reverse when we reverse the light propagation in the microfiber (movie S10). This is also inconsistent with the characteristics of rotation driven by the optical force. (iii) The optical force in the plate-microfiber system is calculated as in the range of pN, which is rather small compared with the friction force (in the range of  $\mu\text{N}$ ). Therefore, the optical force cannot overcome the friction force to drive the gold plate to rotate.

#### **Section S4. A theoretical model of locomotion resolution**

According to the rule of thumb, locomotion resolution can be estimated from the vibration amplitude of the surface acoustic wave (26). The wave amplitude, namely, the elastic deformation in thickness of the gold plate due to photothermal expansion, can be calculated through photothermal simulation.

Firstly, electromagnetic simulation is performed. We used the commercial software FDTD solutions (v8.13, Lumerical) to calculate the electric and magnetic field distributions of the gold plate-microfiber with 3D simulations. Although the gap between the gold plate and the microfiber is unknown to us in the experiment, we chose the gap between the gold plate and microfiber as 1 nm in all simulations according to the estimated gap value from the Van der Waals force calculation in the section S1. It is also within Debye length which is usually used in calculations for the typical length in the electrostatic interaction (36). We used a grid size (dx, 30 nm; dy, 6 nm; dz, 30 nm) for the gold plate-microfiber structure (fig. S3B). In order to appropriately reduce both the simulation memory and simulation time, we tuned the grid size in simulation and find

this value is fine enough for the accuracy of calculations. The bandwidth of supercontinuum light source is 450 nm ~ 2,400 nm. We used 50 wavelengths with an interval of 39 nm. The parameters of the gold plate and the microfiber in simulations is the same as those in movie S4. In experiments, unpolarized light sources are used, so we consider that both fundamental mode  $\text{HE}_{11}^{\text{Vertical}}$  and  $\text{HE}_{11}^{\text{Horizontal}}$  account for 50 percent in simulations. The input time average power of the pulsed laser is 0.4 mW.

Secondly, from the results of FDTD simulations, electric field distribution in the gold plate can be extracted and the heat power volume density  $Q_d(r, \lambda)$  can be calculated as (37)

$$Q_d(r, \lambda) = 0.5 \varepsilon_0 \omega \text{Im}(\varepsilon_r) |E(r, \lambda)|^2 \quad (3)$$

where  $\varepsilon_0$  is the vacuum permittivity;  $\omega$  is the frequency of light source;  $\text{Im}(\varepsilon_r)$  is the imaginary part of the relative permittivity of the gold.  $E$  is the electric field in the gold plate. The light absorptance (fig. S3C) then can be calculated using volume integral of  $Q_d(r, \lambda)$ . For a nanosecond light pulse, the heat source can be described by a Gaussian pulse function as (37)

$$Q_d(r, t) = Q_d(r) \cdot M / (\sqrt{\pi} \tau) \cdot \exp(-(t - t_0)^2 / \tau^2) \quad (4)$$

where  $Q_d(r)$  is the time average heat power (i.e., heat power calculated using the continuum wave source) (fig. S3L);  $M = 50 \mu\text{s}$  is the period of the pulsed light source (i.e. repetition rate 20 kHz);  $\tau = 1.5 \text{ ns}$  is the time constant of the light pulse (calculated according to the pulse duration 2.6 ns);  $t_0 = 3 \text{ ns}$  is the time delay of the pulse peak.

Then the transient temperature  $T(r, t)$  can be calculated using the heat conduction equation



$$C\partial T(r,t)/\partial t + \nabla \cdot (k\nabla T(r,t)) = Q_d(r,t) \quad (5)$$

where  $C$  and  $k$  are the thermal capacity and thermal conductivity, respectively. *COMSOL Multiphysics* software is used to solve this equation. The thermal conductivity of the gold plate with a thickness 30 nm is taken as (38) 150 W/(m·K). The peak of the transient temperature turns to be about 778 K (fig. S3M).

Finally, the expansion of the gold plate in thickness during one light pulse can be calculated as  $\delta d = \alpha \times \Delta T \times d$ , where  $\alpha$ ,  $\Delta T$ , and  $d$  are thermal expansion coefficient, temperature increment, and thickness of the gold plate, respectively. The peak of the transient temperature is 778 K as mentioned above. The thermal expansion coefficient (TEC) of the gold plates (17) is  $31.5 \mu\text{·K}^{-1}$ . For the experimental results in movie S4, the thickness of the gold plate is 30 nm and the maximum expansion of thickness can thus be estimated as 0.46 nm. The theoretical locomotion resolution is then largely estimated as 0.46 nm, which is comparable to the experimental locomotion resolution 0.28 nm.

The absorptance spectrum (fig. S3C) shows that surface plasmonic polaritons (SPPs) should be excited in the gold plate. We calculate two fundamental optical modes in the microfiber. One is the fundamental mode  $\text{HE}_{11}^y$  of which the electric field is in the y direction ( $E_y$ ), perpendicular to the surface of the gold plate. The other is the fundamental mode  $\text{HE}_{11}^z$  with the electric field parallel to the surface of the gold plate ( $E_z$ ). SPPs are excited only when the optical mode in the microfiber is the fundamental mode  $\text{HE}_{11}^y$ . It is due to the fact that electric field perpendicular to the metal surface is necessary to excite the SPPs (41). SPPs do not exist for the fundamental mode  $\text{HE}_{11}^z$ . The plasmonic wavelength locates at  $\lambda_2 = 0.85 \mu\text{m}$ . The electric field is mainly distributed

in the microfiber for the fundamental mode  $HE_{11}^z$  (fig. S3, H to K), while part of electric field is concentrated near the surface of the gold plate for the fundamental mode  $HE_{11}^y$  (fig. S3, D to G). Specially, the electric field is enhanced by a factor of 6 and mainly concentrated near the surface of the gold plate at the plasmonic wavelength (fig. S3, F and G). The plasmonic mode excited in the gold plate play a major role in our experiment by enhancing absorption and thus heating the gold plate more efficiently.

### **Section S5. Numerical simulations of the Lamb wave in an asymmetrically configured plate**

The process of generation of the acoustic wave (i.e. the Lamb wave) in the gold plate excited by the pulsed light can be described as follows (as shown in fig. S8A). First, pulsed light is guided into the microfiber. An exponentially decaying evanescent field is distributed near the microfiber surface. The evanescent field interacts with the gold plate on the surface of the microfiber and the plasmonic mode is excited on the surface of the gold plate, thus enhancing the light absorption of the gold plate. This absorbed light heats the gold plate and the local temperature of the gold plate increases. The temperature of the gold plate changes in the nanosecond time scale (controlled by the nanosecond pulsed light), leading to a sudden expansion and contraction of the gold plate. The Lamb wave is then generated in the plate with this sudden plasmonic photothermal excitation (39). We present a two-dimensional thermoelastic model to analyze the behavior of the Lamb wave for the asymmetric configuration of the plate. To simulate the pulsed-laser-induced Lamb wave, the coupled thermal and elastic wave equations have to be solved simultaneously. The acoustic wave equation with an external force resulting from thermoelastic deformation mechanisms can be described as (40)

$$\rho \frac{\partial^2 \mathbf{u}}{\partial t^2} = \nabla \cdot \mathbf{s} = \nabla \cdot (\mathbf{C} : (\boldsymbol{\varepsilon} - \alpha (T - T_0))) \quad (6)$$

where  $\mathbf{u}$  is the displacement vector;  $\mathbf{s}$  and  $\boldsymbol{\varepsilon}$  are defined as the total stress and total strain tensors;  $\alpha$  is the thermal expansion tensor;  $T$  and  $T_0$  are the object temperature and reference temperature;  $\mathbf{C}$  is the fourth order elasticity tensor related to shear and bulk modulus.

COMSOL Multiphysics software is used to solve this fully coupled system with the heat-transfer module and the structural mechanics module. The required heat source (i.e. a heat power density distribution  $Q_d(x, y, t)$  of the gold plate ) for the heat-transfer module can be obtained from the previous photothermal simulation results (fig. S3L) which can be described as

$$Q_d(x, y, t) = A \cdot \exp(-(t - t_0)^2 / \tau^2) \cdot \exp(-(x - x_0)^2 / s_x^2) \cdot \exp(-y^2 / s_y^2) \quad (7)$$

As shown in fig. S8B, heat power density is maximum at the contact point (of which the coordinate on xy plane is  $(x_0, 0)$ ). It attenuates exponentially along the x and the y direction in the gold plate with a damping factor of  $1/s_x$  and  $1/s_y$ , respectively.  $\tau = 1.5$  ns is the time constant of the light pulse;  $t_0 = 3$  ns is the time delay of the pulse peak.  $A$  is the normalization factor.

Three cases are considered: (1) “right shifted” asymmetric configuration, (2) symmetric configuration, and (3) “left shifted” asymmetric configuration (fig. S8A). The thickness and length of the gold plate in simulations are 30 nm and 20  $\mu\text{m}$ , respectively. The contact point or local heat source generated by absorbing light is arbitrarily chosen to be at the left side ( $x_0 = -7.5$   $\mu\text{m}$ ), in the middle ( $x_0 = 0$   $\mu\text{m}$ ), and at the right side ( $x_0 = 7.5$   $\mu\text{m}$ ) of the gold plate for these three cases, respectively (fig. S8B). The simulation results show that both the temperature evolution and y-displacement evolution at the contact point are basically the same for these three cases. However, the x-displacement evolution at the contact point are totally different for these three cases (fig. S8D). The x-displacement is negative in the “right shifted” asymmetric configuration case. In this case, the motion pattern of the contact point is in the clockwise direction in the xy

plane (see fig. S9B which is obtained by combining fig. S8D and fig. S8E). This implicates that the resultant Lamb wave propagates from the left side to the right side along the gold plate (fig. S9A). In contrast, the x-displacement is positive for the “left shifted” asymmetric configuration case. In this case, the wave pattern of the contact point follows an anticlockwise motion in the xy plane (fig. S9B). This again indicates that the resultant Lamb wave propagates from the right side to the left side along the gold plate (fig. S9A). There is no displacement in the x direction at the contact point in the symmetric configuration case. The deformation evolution of the gold plate at the bottom surface caused by the Lamb wave in the “right shifted” case is shown in fig. S8F. This result shows that the Lamb wave is generated initially at the contact point. The generated Lamb wave then propagates along the two sides of the gold plate (with respect to the contact point) and is reflected back at the boundary.

In order to gain more insight into the origin of these different results in different plate-fiber configurations, we perform an additional simulation (fig. S10). We keep the thickness of the gold plate the same (30 nm) but consider the length of gold plate to be 200  $\mu\text{m}$ . The larger length (compared to the wavelength of the Lamb wave) of the plate demonstrates the wave propagation dynamics more clearly. Although the length of the gold plate is not consistent with the size in the experiment this time, the Lamb wave properties basically remain unchanged. The Lamb wave is generated at the contact point and propagates into two sides of the gold plate (fig. S10B). The Lamb wave propagating to the left is reflected back earlier (after reaching the boundary of the gold plate) compared to the right one, as the distance between the contact point and the left boundary is shorter compared to the right. The displacement of the gold plate at the contact point in the x direction keep zero until the left side Lamb wave is reflected back and reaches the contact point ( $t \approx 24$  ns). After it passes the contact point, the displacement in the x direction becomes negative (fig. S10C). From the results, the velocity and wavelength of the Lamb wave generated in the gold plate excited by a nanosecond laser are  $2.1 \times 10^3$  m/s and 12  $\mu\text{m}$ , respectively.

## Supplementary Figures

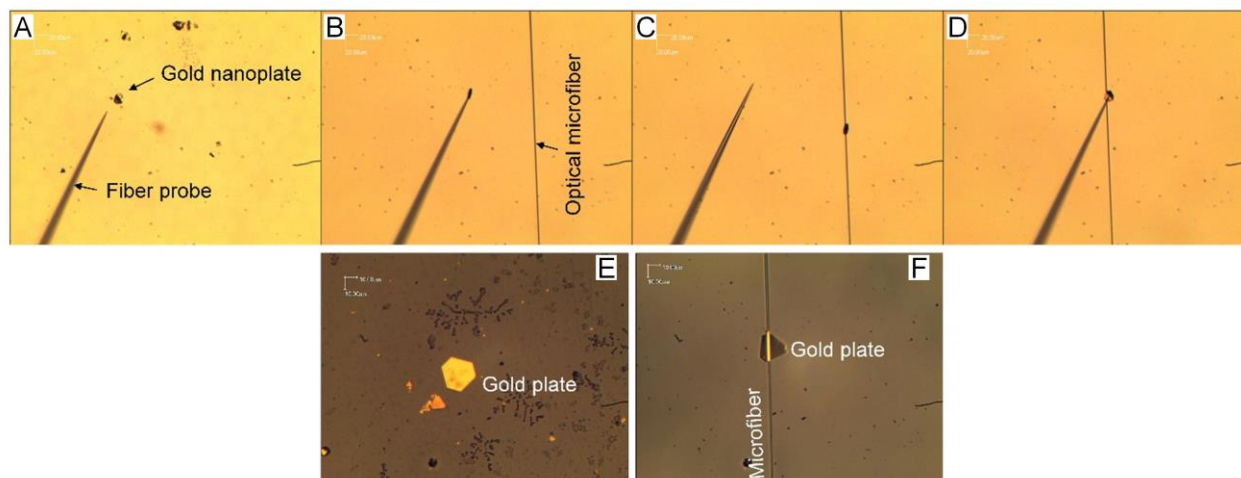


**Fig. S1. Experimental procedures.** (A) Using a tapered fiber probe to pick up a gold plate on a silica substrate. (B) Transferring the gold plate to an optical microfiber suspended in air. (C) The gold plate is transferred to the microfiber successfully. (D) Taking the gold plate off the microfiber after light-actuated rotation experiments. (E and F) Optical images (which are taken from a reflected light microscopy) showing that a gold plate on the silica substrate (E) and on a microfiber which is suspended in air (F).

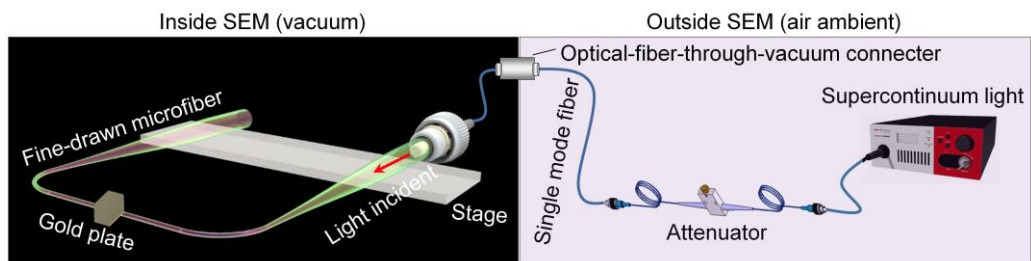


**Fig. S2. Experimental configuration of the locomotor system in vacuum.** The gold plate-microfiber system is put into SEM chamber and the microfiber is connected with the light source outside the chamber by an optical-fiber-through-vacuum connector.

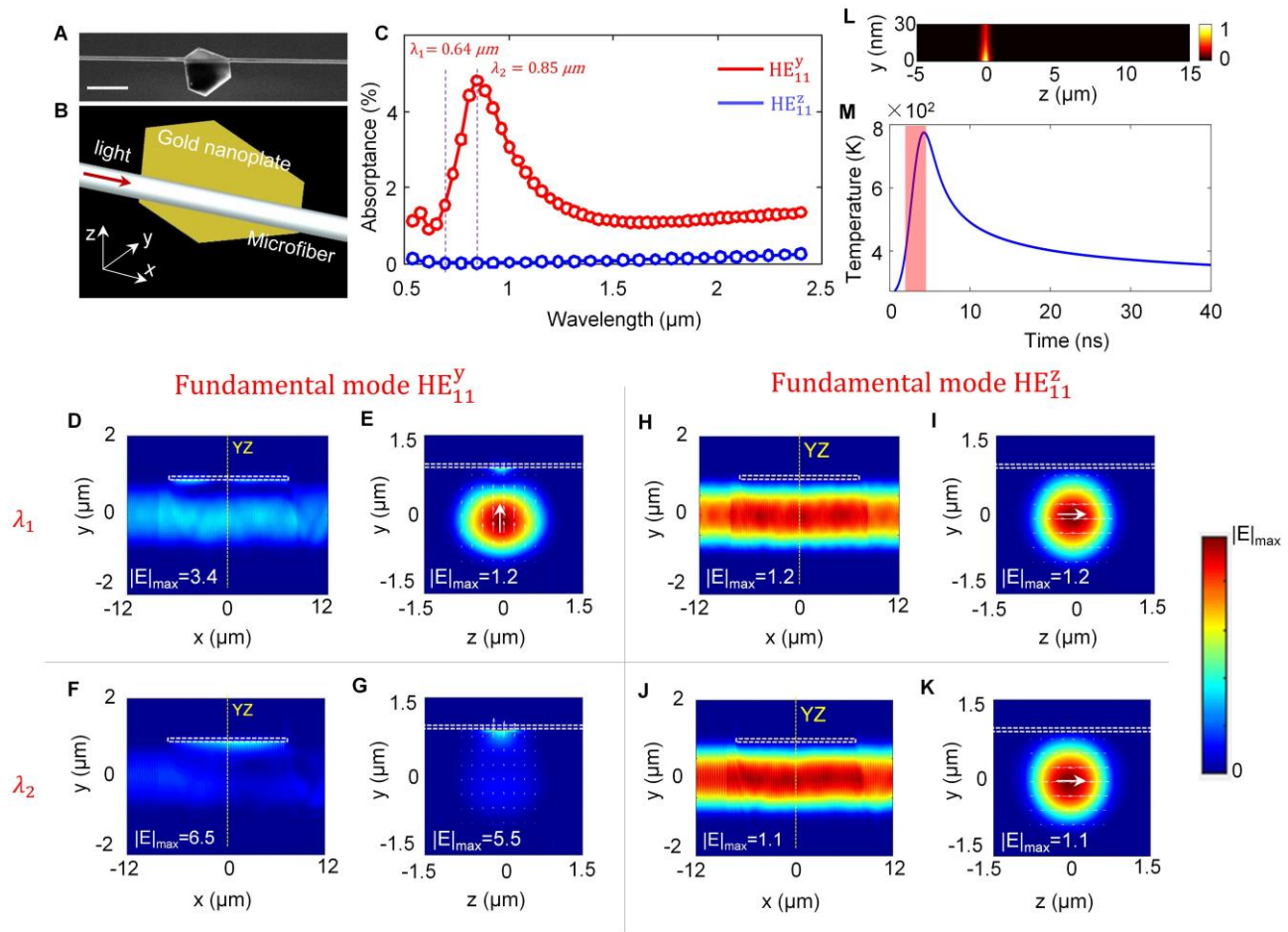


**Fig. S3. Numerical calculation of plasmonic heating in the gold plate.** (A) SEM image of the gold plate-microfiber system in Video S4. Scale bar is 20  $\mu\text{m}$ . (B) Schematic of the plate-microfiber in the numerical model. In simulations, long side length, short side length, and thickness of the gold plate are 15  $\mu\text{m}$ , 9  $\mu\text{m}$ , and 30 nm, respectively. The radius of the microfiber is 900 nm. These parameters are the same as that in Video S4. (C) Calculated spectra of the absorptance of the gold plate. The peak wavelength of plasmonic heating locates at  $\lambda_2 = 0.85 \mu\text{m}$ . (D to K) Simulated electric field distributions of the plate-fiber system when the optical modes in the microfiber are the fundamental mode  $\text{HE}_{11}^y$  (D, E, F, and G) and the fundamental mode  $\text{HE}_{11}^z$  (H, I, J, and K) and the wavelengths are  $\lambda_1 = 0.64 \mu\text{m}$  (D, E, H, and I) and  $\lambda_2 = 0.85 \mu\text{m}$  (F, G, J, and K). The white dashed rectangles in (D-K) indicate the gold plate. White arrows in (E, G, I, and K) indicate the electric vectors. Yellow dashed lines in (D), (F), (H), and (J) indicate the cut planes plotted in (E), (G), (I), and (K), respectively. (L) Calculated normalized heat power density distribution in the gold plate (in YZ plane). (M) Calculated transient temperature at the center of the gold plate. The red zone in (E) indicates light pulse duration time.

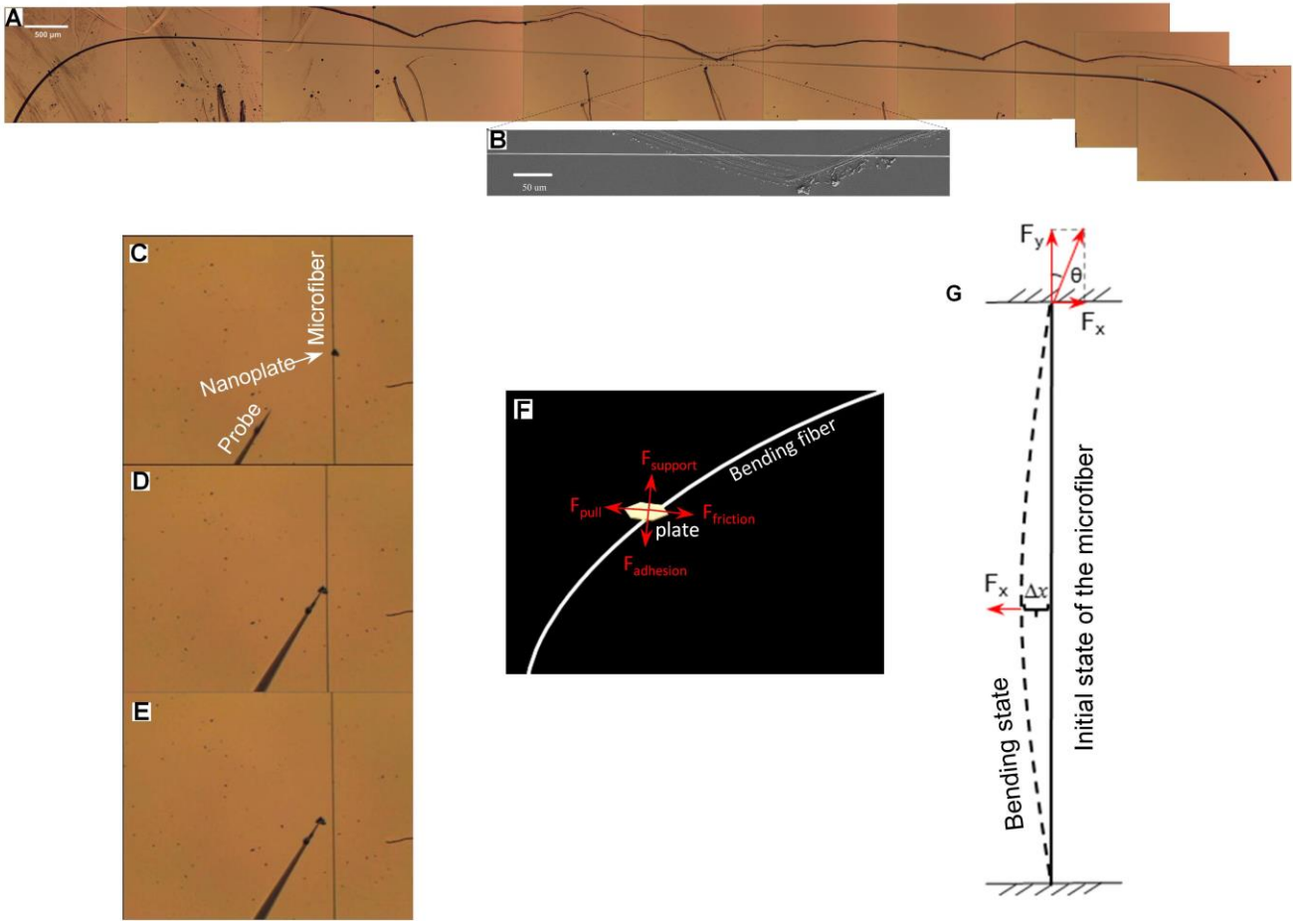


**Fig. S4. Measurements of the adhesion force between gold plates and microfibers.** (A) Optical microscopy image (almost full view) of the microfiber, which is stitched from 11 optical images. (B) SEM image of the middle part of the microfiber in (A). Note that the microfiber is placed on a silicon substrate to characterize its shape and size. (C) Initial state of the microfiber. (D) Bending state of the microfiber (it is when the plate is just to be detached from the microfiber). Microfiber bends to the left when the probe touches with the plate and moves to the left (see video S7). (E) Microfiber restored to the initial state after detaching. The length  $L$  and the effective diameter  $d$  of the whole fiber are 14 mm and 36  $\mu\text{m}$ , respectively. (F) Schematic diagram showing the bending of the microfiber when the plate is pulled by a fiber probe. (G) A simplified model to analyze the forces applied to the bent microfiber in a force-balanced state in (D). The adhesion force is calculated estimated to be 6.9  $\mu\text{N}$ .



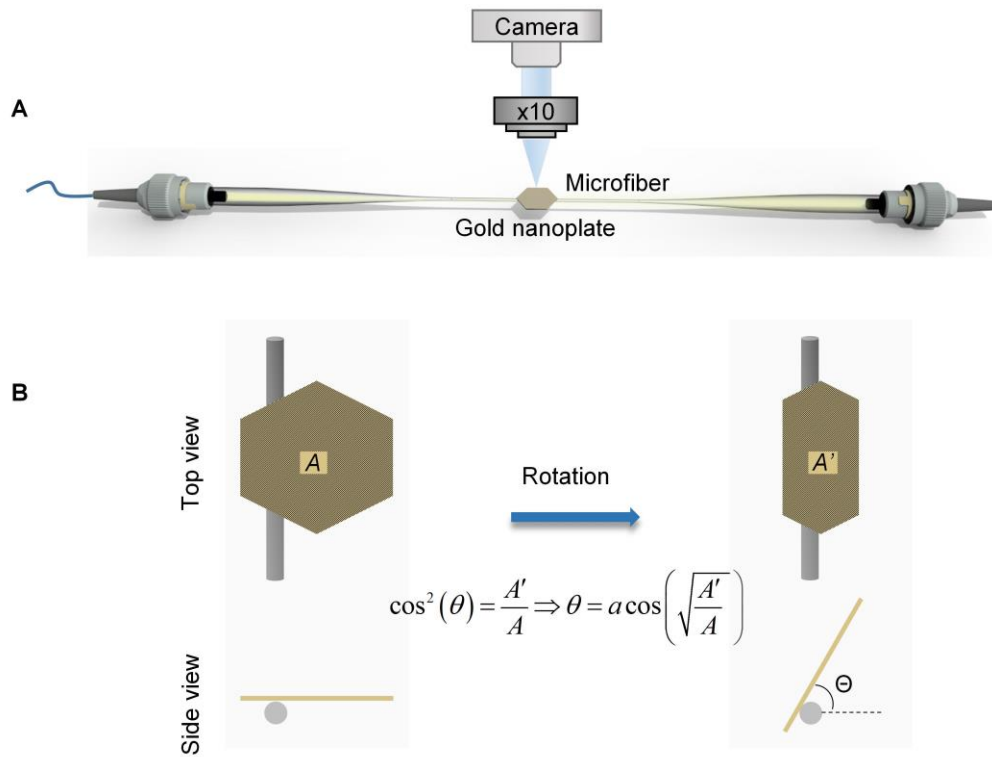


**Fig. S5. Calculations of the angle between the gold plate and the microfiber using the projection method.** (A) Schematic of the experimental configuration. Optical microscope with a camera is used for observation from the top view of the plate-microfiber system. (B) Schematics showing that the gold plate rotates from the initial position “0” to position “ $\theta$ ”. The effective length of the gold plate is defined as  $W_{eff} = \sqrt{A} \cos(\theta)$  and the angle between the gold plate and the microfiber can be calculated with the equation  $\theta = a \cos\left(\sqrt{A'/A}\right)$ . The area of the gold plate ( $A$  or  $A'$ ) can be obtained from every frame in experimental videos. For convenient, the size of the gold plate is presented with pixel length and the unit of area of the gold plate is *square of pixel* ( $pixel^2$ ).

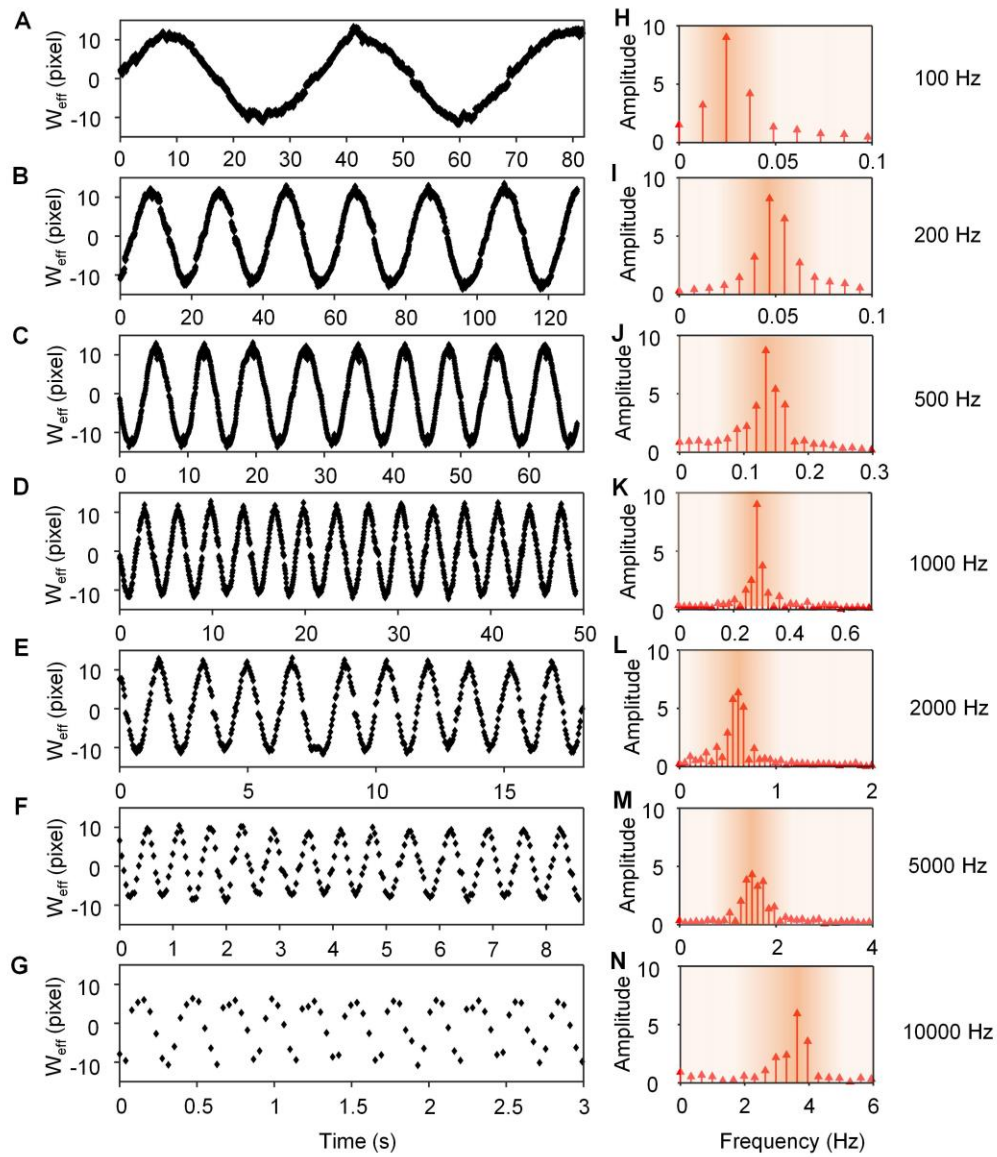


**Fig. S6. Rotation of the locomotor actuated by light pulses with different repetition rates.** (A to G) Effective width ( $W_{eff} = \sqrt{A} \cos(\theta) = \sqrt{A} \cos(\omega t)$ ) of the gold plate (Sample A in Fig. 2) changes periodically over time  $t$ .  $A$  is the area of the gold plate when the angle between the gold plate and the microfiber is zero; see also Extended Data Fig. 5.  $\omega$  is the rotational angular frequency of the plate. (H to N) Fourier transformation of the effective width to obtain the frequency of change of effective width (i.e. rotation speed of the plate). For example, the rotation speed of the gold plate is  $0.29 \pm 0.02$  Hz ( $16.8 \pm 1.2$  rpm) in (K). Repetition rate of light pulses is 100 Hz in (A and H), 200 Hz in (B and I), 500 Hz in (C and J), 1 kHz in (D and K), 2 kHz in (E and L), 5 kHz in (F and M), and 10 kHz in (G and N). The error bars for the measured effective area of the plate is about 6 percent. The orange shades in (H to N), which present the approximate distribution interval of the rotation frequency of the gold plate, are guide to the eyes.

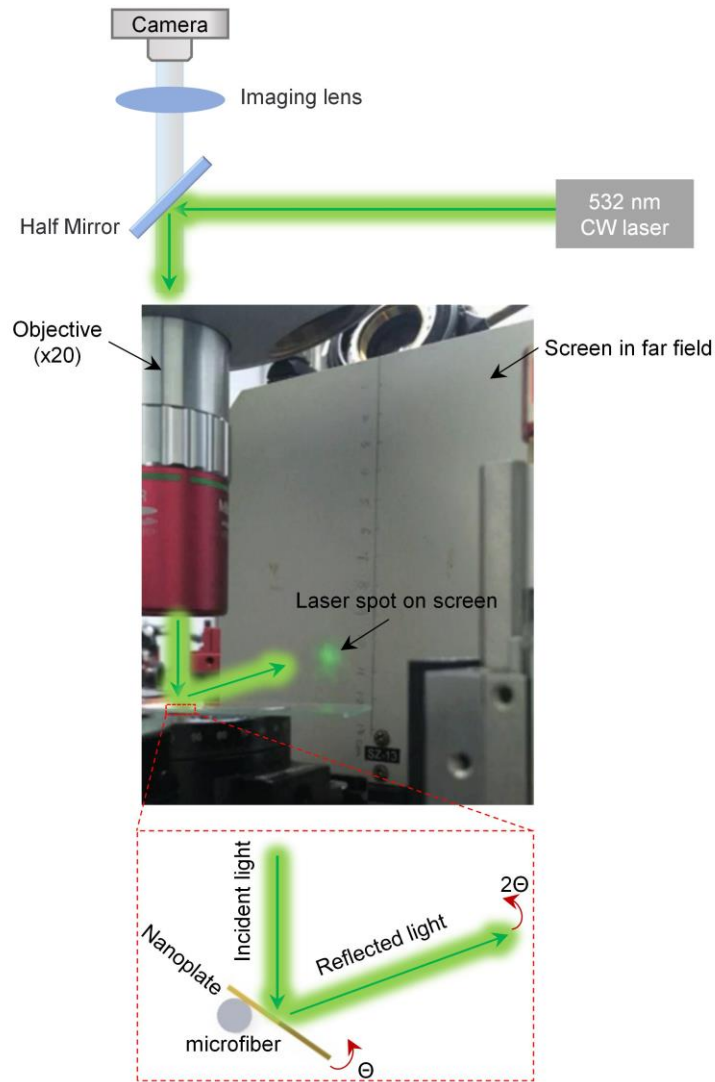


**Fig. S7. Experimental system of a micromirror for optical sweeping.** Camera, imaging lens, and objective are used for observation of the plate-microfiber system. Half mirror and objective is used for focusing a 532 nm CW laser on the plate. White screen is used for displaying projected laser spot from the laser beam reflected by the plate. Credit: the experimental photo in fig. S7 is taken by Jinsheng Lu with a camera of a smartphone (iPhone SE).

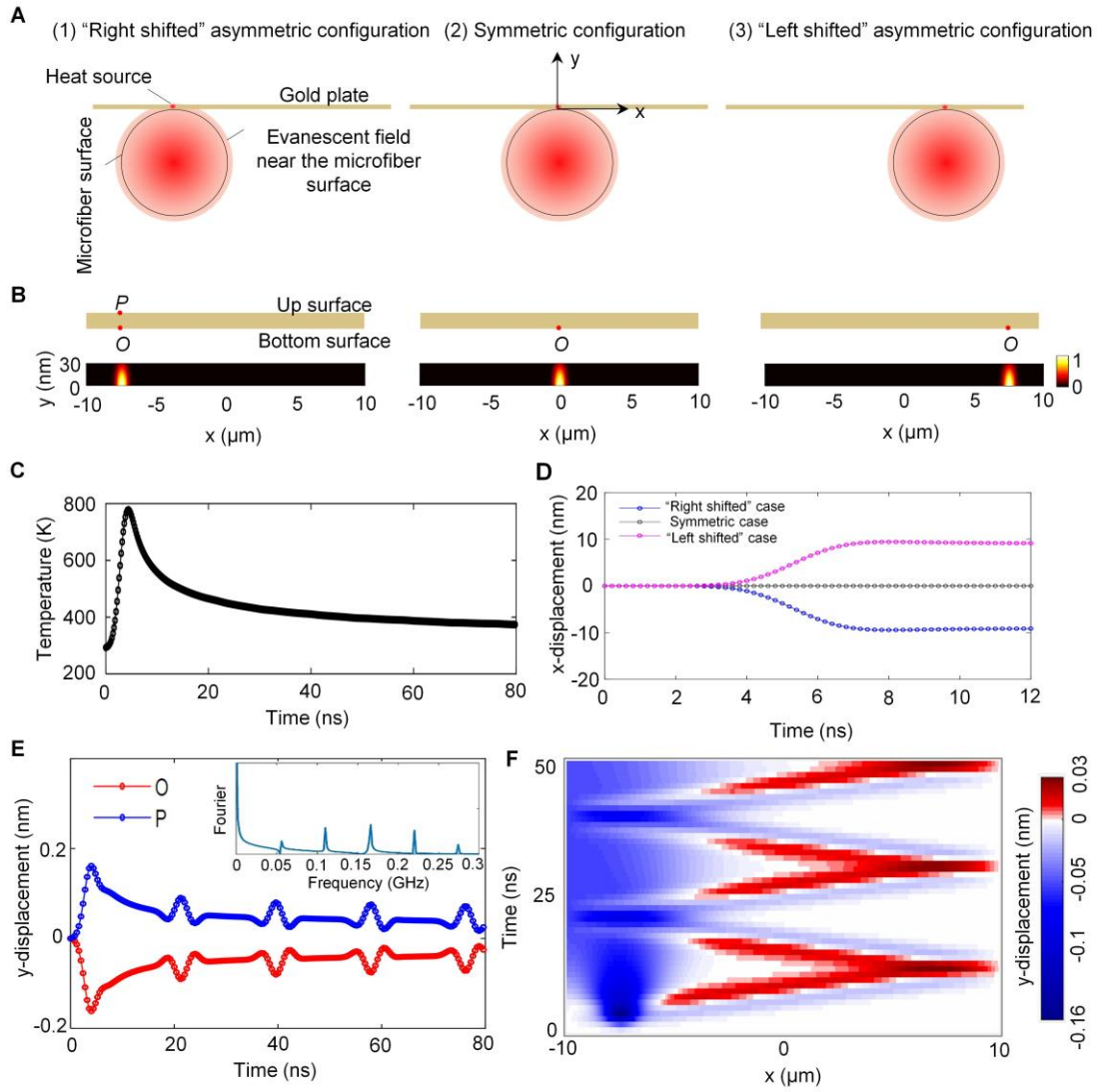


**Fig. S8. Numerical results of the Lamb wave generated in a gold plate.** (A) Schematics of the three cases of the gold plate-microfiber configuration (from left to right: "right shifted" asymmetric configuration, symmetric configuration, and "left shifted" asymmetric configuration). (B) Heat power density distribution in the gold plate in these three cases. The red point  $O$  in (B) indicates the contact point on the gold plate with the microfiber, and  $P$  is the point on the upper surface of the gold plate with the same x-axis coordinate of  $O$ . (C) Calculated temperature evolution of the gold plate at the contact point  $O$ . (D) Calculated displacement evolution of the gold plate at the contact point  $O$  in the x direction for the three cases ("right shifted" asymmetric, symmetric, and "left shifted" asymmetric). (E) Displacement of the gold plate at the contact point  $O$  (on the bottom surface) and point  $P$  (on the up surface) in the y direction. The displacements on the bottom and upper surface are symmetric, and therefore it generates a symmetric Lamb wave. The inset figure in (E) is the Fourier transfer of the y-displacement data in (E). (F) Displacement evolution of the gold plate in the y direction on the bottom surface in the "right shifted" case.

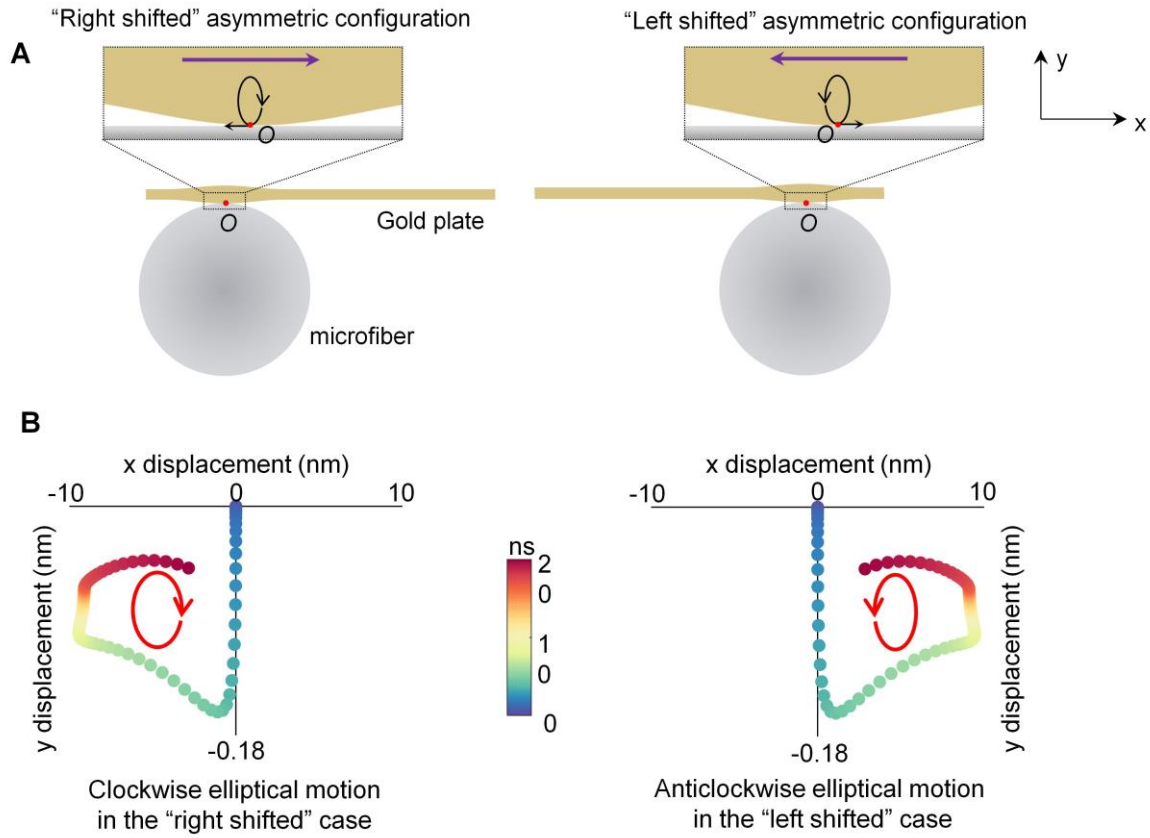


**Fig. S9. Wave motion patterns for the right-shifted and left-shifted asymmetric**

**configurations.** (A) Schematics showing that the Lamb wave propagates from left to right (from right to left) and the contact point on the gold plate forms a clockwise (an anticlockwise) elliptical motion in the “right shifted” case (in the “left shifted” case). (B) Displacement evolution of the gold plate at the contact point  $O$  in the  $xy$  plane for the two different asymmetric configurations. The displacement evolution in  $xy$  plane shows the contact point follows a clockwise motion in the “right shifted” case and follows an anticlockwise motion in the “left shifted” case.

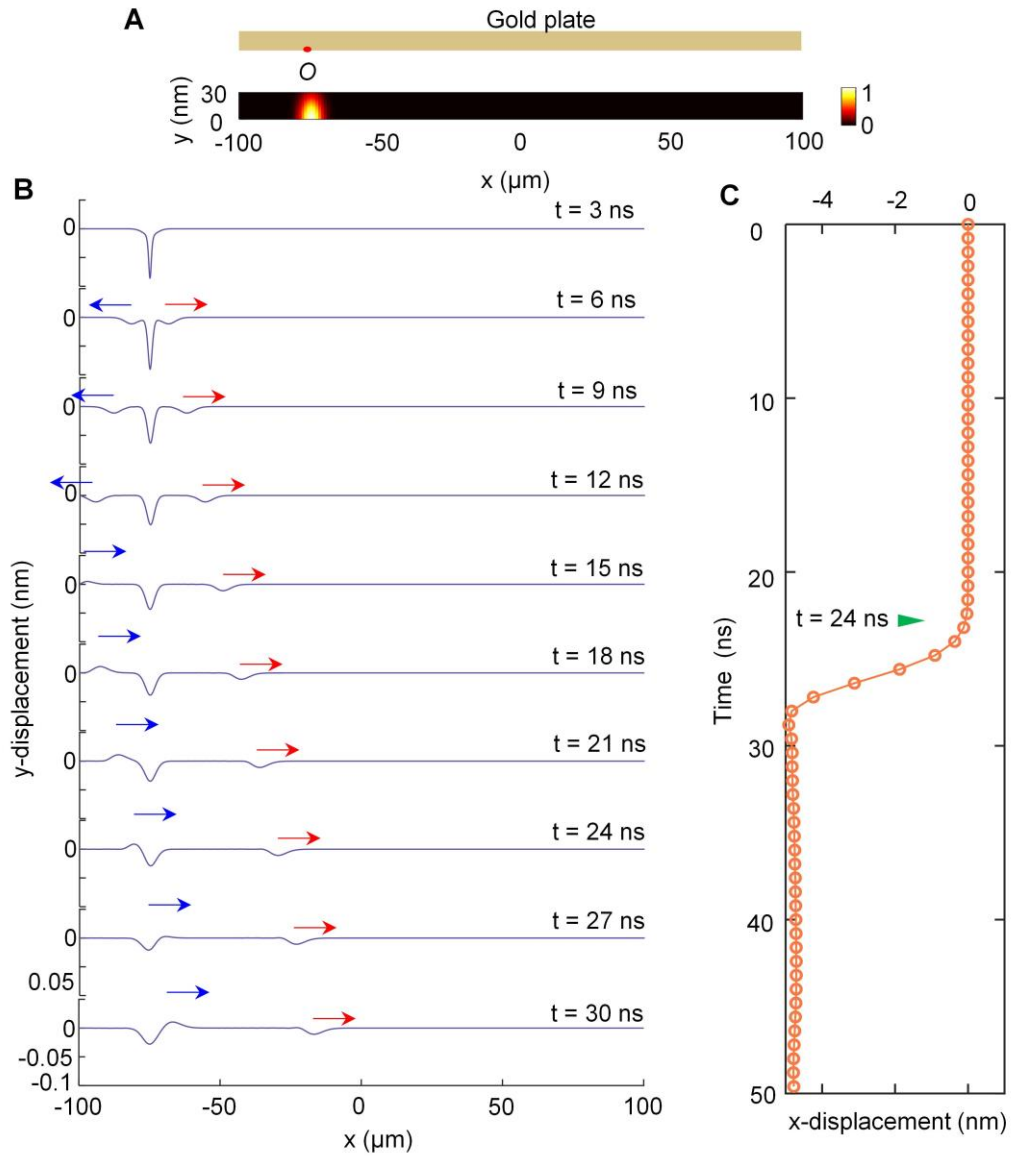


**Fig. S10. Lamb wave propagating in a larger gold plate.** (A) Schematic of a gold plate in “right shifted” case (up) and corresponding heat power density distribution in the gold plate (bottom). In this simulation, the thickness and the side length of the gold plate are 30 nm and 200  $\mu\text{m}$ , respectively. (B) Displacement evolution of the gold plate (in (A)) on the bottom surface. (C) Displacement evolution of the gold plate in (A) at the contact point O in the x direction.

## **Movies (S1-S10) Captions**

**Movie S1. A motor that is driven by a pulsed supercontinuum light with different repetition rates in air (sample A).** This video includes six parts (repetition rate of 5 kHz, 2 kHz, 1 kHz, 500 Hz, 100 Hz, and 10 Hz). Light propagation direction in the microfiber is from bottom to up. Videos are played in real time.

**Movie S2. A motor that is driven by a pulsed supercontinuum light in vacuum.** Light propagation direction in the microfiber is from left to right. Videos are played in real time.

**Movie S3. A pulsed light-actuated stepping motor.** This video includes seven parts (light pulses burst number 1000, 500, 200, 100, 50, 10, and 1). The light pulses burst comes every second. Light propagation direction in the microfiber is from bottom to up. Videos for light pulses burst number 1000, 500, 200, 100, 50 are played in real time. Videos of which the light pulses burst number is 10 are played at 5 times speed. Videos of which the light pulses burst number is 1 are played at 10 times speed.

**Movie S4. A lower power of the light pulse and a smaller rotation step for the locomotor.** The rotation direction is anticlockwise, and the rotational speed is 60 rpm (1 Hz). The long side length and the short side length of the hexagonal gold plate are 15  $\mu\text{m}$  and 9  $\mu\text{m}$ , respectively. The thickness is 30 nm. The diameter of the microfiber is 1.8  $\mu\text{m}$ . The measured average optical power is 0.4 mW and the repetition rate of light pulses is 20 kHz. Videos are played in real time.

**Movie S5. A motor that is driven by a 1064-nm pulsed light in air.** The side length of the hexagonal gold microplate is 13  $\mu\text{m}$ , and the diameter of the microfiber is 3.0  $\mu\text{m}$ . Videos are played in real time.

**Movie S6. A motor that is driven by a pulsed supercontinuum light with different repetition rates in air (sample B).** This video includes four parts (repetition rate of 10 kHz, 5 kHz, 2 kHz, and 1 kHz). The size of the gold plate is 8.6  $\mu\text{m}$ , and the diameter of the microfiber is 1.9  $\mu\text{m}$ . Light propagation direction in the microfiber is from bottom to up. Videos are played in real time.

**Movie S7. Deforming the microfiber to measure the adhesion force.** The length of the microfiber is 14 mm. The effective diameter of the microfiber is 6  $\mu\text{m}$ . The maximum deformation ( $\Delta x$ ) is 10  $\mu\text{m}$ . There is no light guided into the microfiber during the process of gold plate detaching. Videos are played in real time.

**Movie S8. An animation to illustrate the rotary locomotion of the motor.** This 3D animation shows that the contact point on the gold plate does not change during the rotary locomotion.

**Movie S9. A light-actuated rotary micromirror.** This video includes two parts. The first part is a rotary plate recorded by the camera. The second part is projected laser spot moving upward on a white screen, which is recorded by the phone camera. Videos are played in real time.

**Movie S10. Rotation direction of the motor controlled by different asymmetric configurations.** This video includes three parts. The first part shows an anticlockwise rotating plate around the microfiber in the “right shifted” asymmetric configuration. The second part shows a clockwise rotating plate around the microfiber in the “left shifted” asymmetric configuration. The third part shows a clockwise rotating plate around the microfiber in the “left shifted” asymmetric configuration with reverse light propagation compared with that in the second part. Videos are played in real time.